Available online at www.sciencedirect.com
SCIENCE DIRECT
Polymer 47 (2006) 6156–6166
polymer
www.elsevier.com/locate/polymer

New insights into rubber–clay nanocomposites by AFM imaging

Madhuchhanda Maiti, Anil K. Bhowmick*

Rubber Technology Centre, Indian Institute of Technology, Kharagpur-721302, India

Received 17 January 2006; received in revised form 10 June 2006; accepted 15 June 2006
Available online 10 July 2006

Abstract

In the present study, topographic and phase imaging in tapping mode atomic force microscopy was performed to investigate the size of clay platelets, the polymer–filler interface, pull-off and contact forces between the sample and the tip, power spectral density, fractal dimension and spatial distribution of the nanoclays [unmodified (Cloisite NA) and modified clay (Cloisite 20A)] in the terpolymer of vinylidene fluoride, hexafluoropropylene and tetrafluoroethylene (fluoroelastomer). The phase images of the above nanocomposites elucidated that the width of clay particles was lower in the case of the unmodified clay filled system. Interestingly, the polymer was able to exfoliate both the unmodified and modified clays. This phenomenon was supported by transmission electron microscopy and X-ray diffraction studies. The results obtained from the section analysis and the histogram of the filler distribution further supported the above findings. The surface roughness was less in the case of the unmodified clay based nanocomposite, as determined from roughness, power spectral density and fractal analysis. The study also indicated an improved particle distribution in the case of the unmodified clay filled samples. The results were explained with the help of thermodynamics and soft–hard acid base theory.

Keywords: AFM; Fluoroelastomer; Clay

1. Introduction

It has been well recognized that the extent of dispersion of nanoclays strongly influences the properties of the polymer/layered-silicate nanocomposites [1–6]. The filler dispersion depends on the nature of matrix as well as nanoclay. In a true nanocomposite, the clay layers must be uniformly dispersed and exfoliated in the polymer matrix, rather than being aggregated as tactoids. But in most of the cases, a nanocomposite having both exfoliated and intercalated morphology is obtained.

Two complementary characterization techniques have been extensively used in the investigation of morphology of polymer–clay nanocomposites, namely X-ray diffraction (XRD) and transmission electron microscopy (TEM). However, certain disadvantages of TEM such as radiation damage and tedious sample preparation are also now well known. In contrast to the conventional electron microscopy, AFM does not require a conductive coating or staining. Hence, AFM analysis of the nanocomposites can be a good alternative to electron microscopy, without any limitations regarding contrast and resolution. The development of this technique has helped to image surface topography on a nanometric scale [7]. Besides, this multifunctional technique is suitable to understand the nanofiller dispersion in the matrix along with surface topography. In addition to the normal topographical imaging, AFM can also measure fundamental properties of sample surfaces, e.g., local adhesive or elastic properties on a nanometric scale. We have earlier reported from this laboratory various AFM investigations on carbon black and silica reinforced polymers [8,9].

Interestingly, in the literature there have been only a few reports on the morphology of rubber–clay nanocomposites by atomic force microscopy (AFM) [10–14]. Literature survey shows that only the morphology of a few nanocomposites was investigated using AFM so far [15–20]. The surface topography and quantitative surface analysis including the

* Corresponding author. Tel.: +91 3222 283180; fax: +91 3222 220312.
E-mail address: anilkb@rtc.iitkgp.ernet.in (A.K. Bhowmick).

0032-3861/$ - see front matter © 2006 Elsevier Ltd. All rights reserved.
doi:10.1016/j.polymer.2006.06.032

nano-range forces present in the composites have not been studied.

Out of three modes of AFM, tapping mode (TMAFM) is the most suitable for soft rubber samples. In this mode, short intermittent tip–sample contact reduces lateral forces, which minimizes sample damage during scanning [21]. In our earlier preliminary report, the morphology of rubber–clay based nanocomposites was investigated by both TEM and AFM [12]. The studies showed a good correlation between TEM and AFM results. But quantitative analysis cannot be done extensively with TEM.

Hence, in the present paper, for the first time, attempts have been made to study the morphology of rubber–clay nanocomposites, nanofiller distribution, interfacial region, contact and adhesion forces using AFM. Fluoroelastomer/clay nanocomposite has been taken as a representative system. The preparation and properties of these nanocomposites, reported elsewhere, indicated outstanding mechanical and dynamic mechanical properties, generally required for space application where this rubber is extensively used [22]. AFM has been used as an effective tool to analyze the morphology qualitatively and also to quantify the surface features of the nanocomposite systems. The scanning probe microscope (SPM) data of virgin rubber film and the nanocomposites were evaluated qualitatively and quantitatively using power spectral density to envisage the effect of different nanoclays on the morphology of the resulting nanocomposites. The interfacial region between rubber and filler has been traced with this tool. Also, the adhesion force at different positions – on the filler particle, interface region and on the matrix – has been determined using contact mode AFM. The latter information was also not reported on the rubber–clay system.

2. Experimental

2.1. Materials used

Viton B-50 [a terpolymer of vinylidene fluoride (VF2), hexafluoropropylene (HFP) and tetrafluoroethylene (TFE), density 1850 kg m^{-3} at 25 °C, 68% F, Mooney Viscosity, ML 1 + 10 at 120 °C = 39] was procured from DuPont Dow Elastomers, Freeport, Texas, USA. Nanoclays namely Cloisite NA+ (NA) and Cloisite 20A (20A) were obtained from Southern Clay Products, Gonzales, Texas, USA. Methyl ethyl ketone was supplied by Nice Chemicals Pvt. Ltd, Cochin, India.

2.2. Preparation of rubber–clay nanocomposites

The rubber was first dissolved in methyl ethyl ketone (20 wt% solution). The clay was dispersed in methyl ethyl ketone (10 wt%). Then the dispersed clay was added to the rubber solution and thoroughly stirred to make a homogeneous mixture, which was then kept in air for 15 days to drive off the solvents slowly. It has been already reported in our earlier paper that at this rubber solution concentration, the clay particles remain well dispersed throughout the matrix even after evaporating the solvent [23]. Here, 4 phr (parts per hundred gram of rubber) of clay was selected as the mechanical properties were optimized at this loading (reported in our earlier paper [22]).

Table 1
Designation of different nanocomposites

Composition	Designation
Viton B-50	F_{B5}
Viton B-50 + 4 phr Cloisite NA+	$F_{B5}C_{NA}4$
Viton B-50 + 4 phr Cloisite 20A	$F_{B5}C_{20A}4$

Table 1 shows various compositions prepared for this investigation and their designation.

2.3. Method

2.3.1. Atomic force microscopy (AFM)

In order to have a very smooth surface for AFM analysis, the samples were first cooled to −60 °C by using liquid nitrogen and then sliced by using a diamond knife attached to a Leica Ultracut UCT cryomicrotome unit. The scanning and analysis of the samples were done using the Multi Mode Scanning Probe Microscope model with a Nanoscope IIIa controller by Digital Instruments Inc. (Veeco Metrology Group), Santa Barbara, CA, USA. The AFM measurements were carried out in air at ambient conditions (25 °C) using tapping mode probes with constant amplitude. The tapping mode etched silicone probe (RTESP) (square pyramid in shape with a spring constant of 20 N/m, nominal radius of curvature of <10 nm) with resonance frequency of 270 kHz was used. Height and phase images were recorded simultaneously at the resonance frequency of the cantilever with a scan rate of 1 Hz and a resolution of 256 samples per line. This allowed the resolution of individual primary particle measurements. Scanning was done at 10 different positions of each sample and representative images have been displayed here. Section analysis, roughness, and power spectral density measurements were done using a nanoscope image processing software (version 5.12 r1). The measurement of roughness, and power spectral density was done on the same size of scan area for comparison purpose.

The adhesion force was determined from force–distance curve obtained from contact mode AFM. The silicon-nitride probe (NP20), having a square pyramidal shape with a spring constant 0.12 N/m was used for this analysis. These cantilevers were precalibrated. Contamination of a probe and a substrate by particulates and adsorbates is a common problem in the AFM laboratories. Hence, high precaution was taken before doing these force measurements. Just before doing these experiments, fresh sample surface was generated by microtoming and new tip for each sample was used. We also scanned the same surface after doing force measurements and observed that there was no artifact due to contamination of tip.

2.3.2. Roughness analysis

The changes in surface topography could be determined quantitatively by the root mean square (RMS) roughness calculation (R_q). This is used in a range of applications

particularly where the surfaces involved show a degree of randomness. The roughness calculation was based on finding a median surface level for the image and then evaluating the standard deviation within the image. Since the roughness analysis was based on the vertical axis, i.e. the z-axis, the topographic height images were used in the present investigation. Root mean square average of height deviations taken from the mean data plane was expressed as [24]:

$$R_q = \sqrt{\frac{\sum (Z_i)^2}{n}} \tag{1}$$

where Z_i is the current Z value, and n is the number of points on the image. Mean roughness, R_a, was the arithmetic average of the absolute values of the surface height deviations measured from the mean plane:

$$R_a = \frac{1}{n}\sum_{j=1}^{n} |Z_j| \tag{2}$$

2.3.3. Power spectral density

In order to understand the surface analysis in the context of PSD, it is necessary to consider surfaces as superposition of spatial waves [25,26]. The variation of height in real space can be considered in terms of power spectrum in frequency space through the use of the Fourier transform, which is a well-known means of relating real space to frequency space. Surface data generated by any instrument can be considered as series of height values, $h(x)$ or $h(y)$, corresponding to spatial positions, x and y. In the one-dimensional (1D) case of $h(x)$, where $H(f)$ is the resulting frequency space profile of the real surface, the Fourier transform was written as [26]

$$H(f) = \frac{1}{L}\int_0^L h(x) e^{(-2\pi i f x)}\, dx \tag{3}$$

where L is the total length of the scan and i is $\sqrt{-1}$. The algorithm used to obtain the PSD depends upon squaring this Fourier transform of the image to derive the power, P. Once the power, P, is obtained, it may be used to derive one-dimensional power spectral density (1DPSD) values as follows [24]:

$$\mathrm{PSD} = \frac{P}{\Delta f} \tag{4}$$

The terms used in the denominators in Eq. (4) are derived by progressively sampling data from the image's two-dimensional Fast Fourier transform center (Fig. 1). Each sampling swings a "data bucket" of given frequency f.

Thus, units of (length)^3 are used for the one-dimensional power spectral density (1DPSD).

The surfaces were analyzed by a series of line scans of N_x steps, yielding a profile, $h(x)$, for each value from 1 to N_y in the y direction. The PSD was then calculated by taking the Fourier transform of each of these line scans, squaring the result to determine the power, and averaging the power calculated for each line scan to generate a single 1DPSD for the surface.

Two-dimensional PSDs (2DPSD) typically use an annular average of the square of two-dimensional Fourier transforms of the surface rather than one-dimensional Fourier Transform. It is expressed as [24]

$$\mathrm{PSD} = \frac{P}{2\pi f(\Delta f)} \tag{5}$$

Two-dimensional power spectral densities (2DPSDs) can be useful for revealing two-dimensional periodicities, such as pores and grains. The transition points or peak values in a 2DPSD are the same in frequency space as the 1DPSD, but the slope of the power-law regime and the absolute magnitude, as well as the units of the surface power are different.

In PSD, the smaller features on a surface as high frequency peaks (short wavelengths) appeared on the right hand side of the spectra and the bigger features were placed on the left hand side of the spectra. Power is roughness amplitude squared and the sum of the power contained in the entire spectrum is called total power.

2.3.4. Infra-red spectroscopy

Infra-red spectroscopy study was done in Perkin–Elmer 843, in the range 400–4000 cm^{-1} using solution process (1% solution of the rubber/nanocomposites in methyl ethyl ketone).

2.3.5. Transmission electron microscopy (TEM)

The nanocomposite samples for TEM analysis were prepared by ultra cryomicrotomy using Leica Ultracut UCT. Freshly sharpened glass knives with cutting edge of 45° were used to get the cryosections of 100 nm thickness. Since

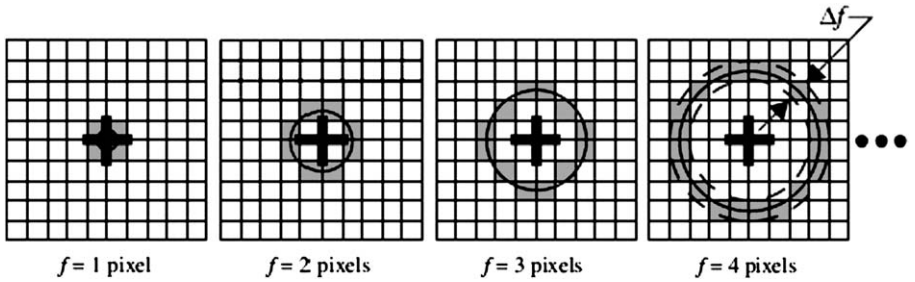

Fig. 1. Progressive data sampling.

these samples were elastomeric in nature, the sample temperature during ultra cryomicrotomy was kept constant at −60 °C [which was well below the glass transition temperature (T_g), of the rubber], at which the samples existed in hard glassy state, thus facilitating ultra cryomicrotomy. The cryosections were collected and directly supported on a copper grid of 200-mesh size. The microscopy was performed later using JEOL-2010 electron microscope (not attached to the cryomicrotomy unit), operating at an accelerating voltage of 200 kV.

2.3.6. X-ray diffraction studies (XRD)

For the characterization of the rubber nanocomposites, XRD studies were performed using a Philips X-Pert Pro diffractometer in the range of 2−9° and Cu-target ($\lambda = 0.154$ nm). Then, *d*-spacing of the clay particles was calculated using the Bragg's law. The samples were placed vertically in front of the X-ray source. The detector was moving at an angle of 2θ while the sample was moving at an angle of θ.

3. Results and discussion

3.1. Particle size and nanofiller distribution

The phase images of the neat rubber, the unmodified and the modified clay loaded samples (F_{B5}, $F_{B5}C_{NA}4$, $F_{B5}C_{20A}4$) are illustrated in Fig. 2a−c. In the case of the clay filled samples, some distinct white bright features are observed, which are absent in the unfilled sample. This suggests that the filler appears as white bright features in the grey rubber matrix. In the tapping mode, the measurement of the difference between the phase angle of the excitation signal and the phase angle of the cantilever response is used to map compositional variations such as stiffness, hardness and viscoelasticity on the sample surface. The variation in the image contrast of the neat rubber and the filled systems can be related to the sample modulus as follows [27]. The phase image can provide a stiffness variation in the sample, which is expressed by the following equation:

$$\Delta\varphi_0 \approx \langle S\rangle \left(\frac{Q}{k}\right) = \varepsilon\langle a\rangle E^* \left(\frac{Q}{k}\right) \tag{6}$$

where, $\Delta\varphi_0$ is the phase angle shift between free and interacting cantilevers, S is the stiffness of the material, Q is the quality factor, which is a measure of viscous damping of the cantilever, k is the spring constant of the cantilever, ε is a constant, a is the radius of the contact area between tip and the surface, and E^* is the effective modulus of the material. $\langle S\rangle$ and $\langle a\rangle$ are time-averaged values of the stiffness S, and contact radius a, over one cycle of oscillation. Hence, a stiffer region will correspond to a greater value of E^* and $\Delta\varphi_0$.

The lower modulus of neat rubber results as dark grey matrix, which may be due to the deeper indentation of the cantilever in the sample. However, phase images of the filled samples exhibit three shade differences: dark grey for the matrix, grey for the matrix near clay particles (interface region) and white for the clay particles. From Fig. 2b,c, it can be clearly seen that the clay particles are well distributed all over the matrix in the case of NA filled system, while in the case of the organoclay filled sample, the clay particles

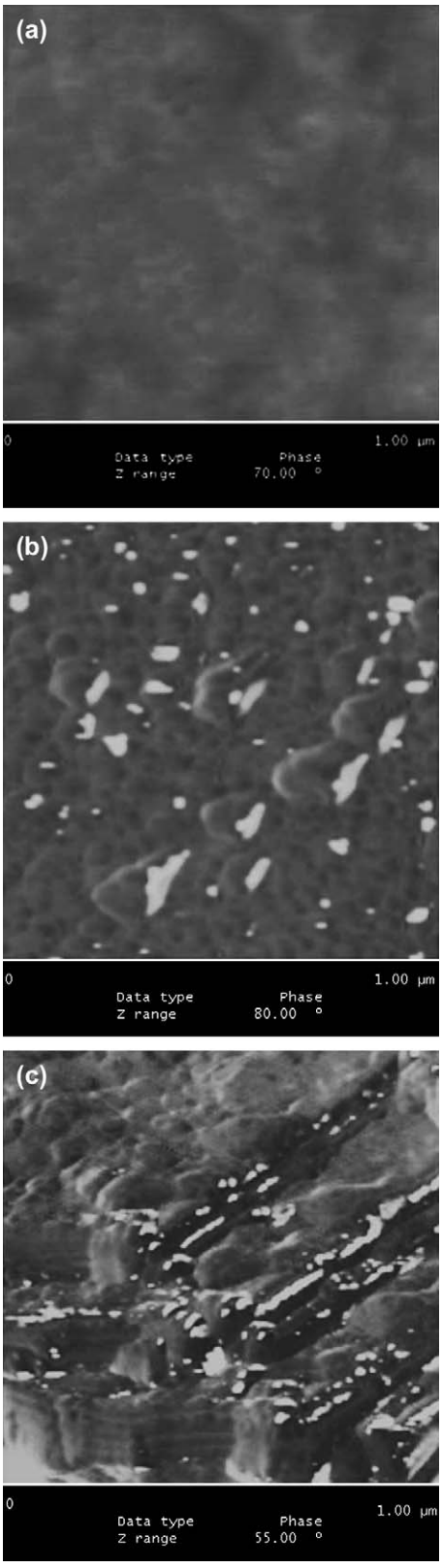

Fig. 2. Phase images of (a) F_{B5}, (b) $F_{B5}C_{NA}4$, and (c) $F_{B5}C_{20A}4$.

are confined to particular portions, not distributed all over the matrix. Similar observation is made when a large number of areas were analyzed at different magnifications. The average particle width is 10 ± 3 nm and 15 ± 2 nm in the case of $F_{B5}C_{NA}4$ and $F_{B5}C_{20A}4$, respectively, excluding the interface region. The average length of the clay filler is 130 ± 20 nm and 110 ± 10 nm in the case of the former and the latter samples, respectively. These features are also observed in the 3D-phase images of $F_{B5}C_{NA}4$ and $F_{B5}C_{20A}4$ in the same scan size (Fig. 3a,b). The transmission electron micrographs also show that both the clays are exfoliated in the matrix (Fig. 4a,b). The unmodified clay particles are having $\sim$1 nm thickness and the modified clay filled samples are having $\sim$5 nm thick platelets. AFM study gives a higher particle thickness which may be due to the tip broadening effect [28]. The exfoliation of both the clays can be further supported by XRD data. The XRD diagram shown in Fig. 5, clearly illustrates the absence of any peak in the diffractograms of both the nanocomposites ($F_{B5}C_{NA}4$ and $F_{B5}C_{20A}4$). The unmodified and the modified clays reveal a peak at $2\theta = 7.5°$ and $2\theta = 3.6°$, respectively [22]. It indicates that the layer structure of the clays has been broken down and the clay platelets are well separated from each other, i.e. the clays are exfoliated.

In order to visualize the particle size and distribution of the clay particles, the samples, mentioned earlier, were subjected to different surface analyses. Fig. 6a–c shows the section analysis of F_{B5}, $F_{B5}C_{NA}4$ and $F_{B5}C_{20A}4$. A cross-sectional line was drawn over the scanned image to select the clay particles. The

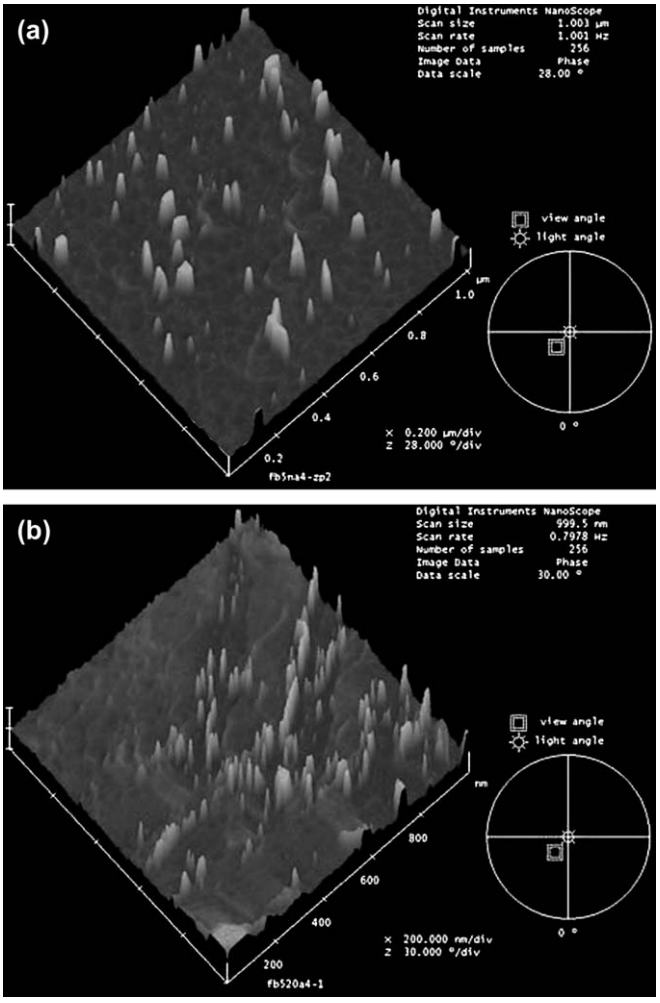

Fig. 3. 3D images of (a) $F_{B5}C_{NA}4$ and (b) $F_{B5}C_{20A}4$.

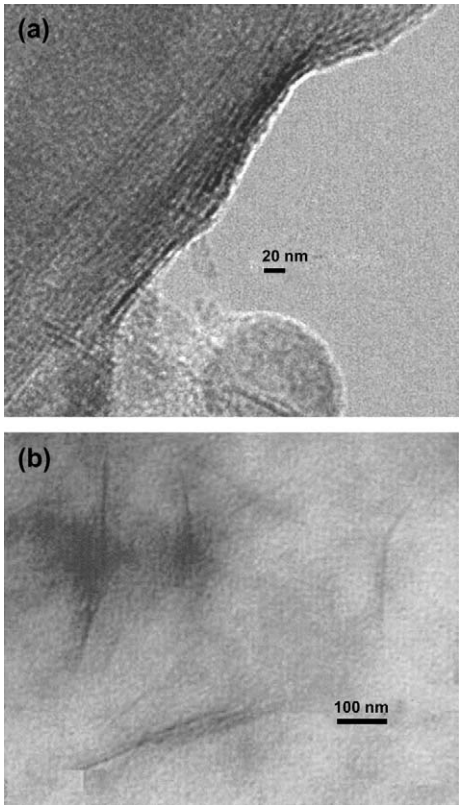

Fig. 4. TEM micrographs of (a) $F_{B5}C_{NA}4$ and (b) $F_{B5}C_{20A}4$.

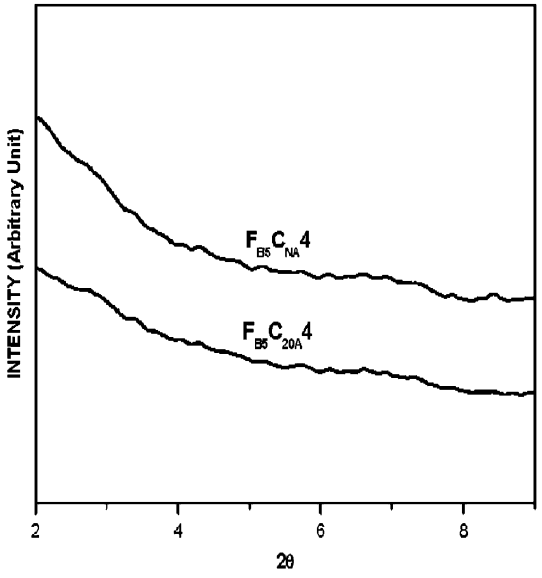

Fig. 5. XRD diffractogram of nanocomposites.

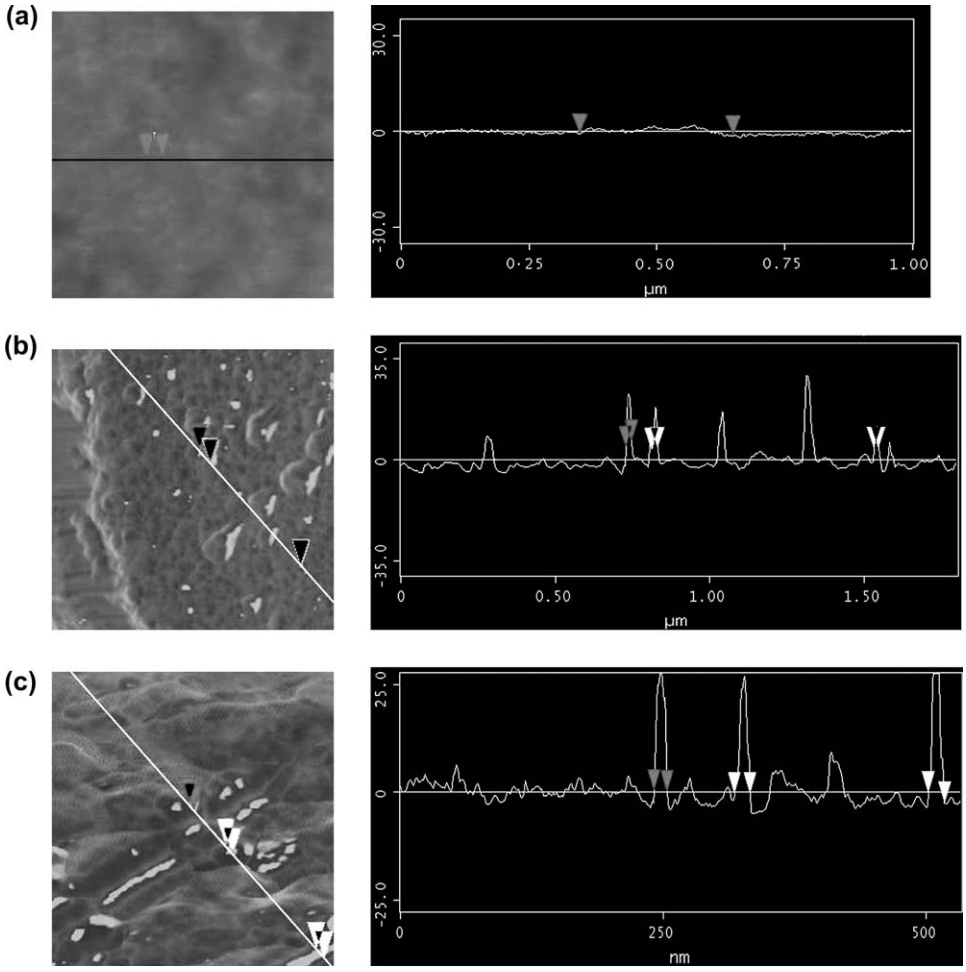

Fig. 6. Section analyses of (a) F_{B5}, (b) $F_{B5}C_{NA}4$, and (c) $F_{B5}C_{20A}4$.

cross-sectional profiles along this reference line are shown as spectra. The projections of the surface irregularities of the filler particles on the rubber matrix and the variation in stiffness along the line are displayed in the form of line spectra. There is no peak transition in the neat rubber matrix, while there are peaks in the filled samples. The average particle width is 10 ± 3 nm and 15 ± 2 nm for the unmodified and the modified clay filled samples, respectively.

In order to understand the filler distribution, histograms are plotted (Fig. 7). In the case of unmodified clay filled sample the maximum is at 0–5 nm, whereas in the case of modified clay filled system, it is at 6–10 nm. Hence, it can be inferred that the average particle size is smaller in the case of the unmodified clay filled systems than the modified clay loaded system. Moreover, with Cloisite NA, it gives broader distribution. Also, the interparticle distance is 310 ± 100 nm and 105 ± 50 nm for the unmodified and the modified clay filled samples, respectively. For the conventional carbon black and silica filled styrene–butadiene rubber-composites, the interaggregate distance (i.e. the distance between the filler-aggregates) is 600 ± 80 nm [8].

The image contrast at the interface (Fig. 8a,b) can be interpreted as follows: interaction between the clay and the rubber makes the rubber chains immobilized around the filler particles. Therefore, the modulus of the rubber near filler particles is higher as compared to bulk of the sample, due to polymer–filler interaction. Compared to the modified clay

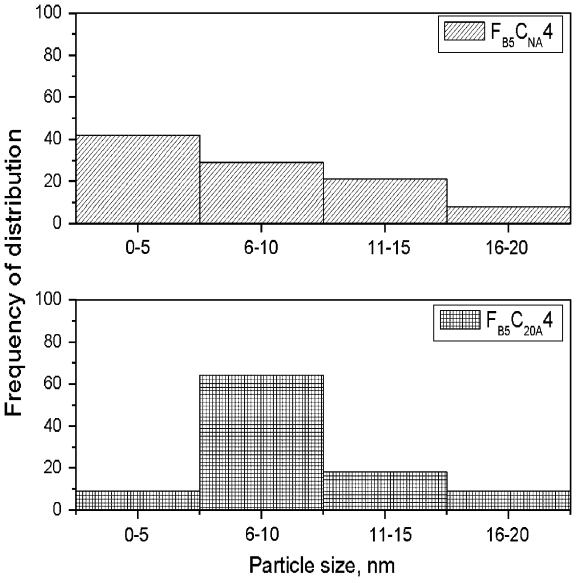

Fig. 7. Histograms showing the particle size distribution in $F_{B5}C_{NA}4$ and $F_{B5}C_{20A}4$.

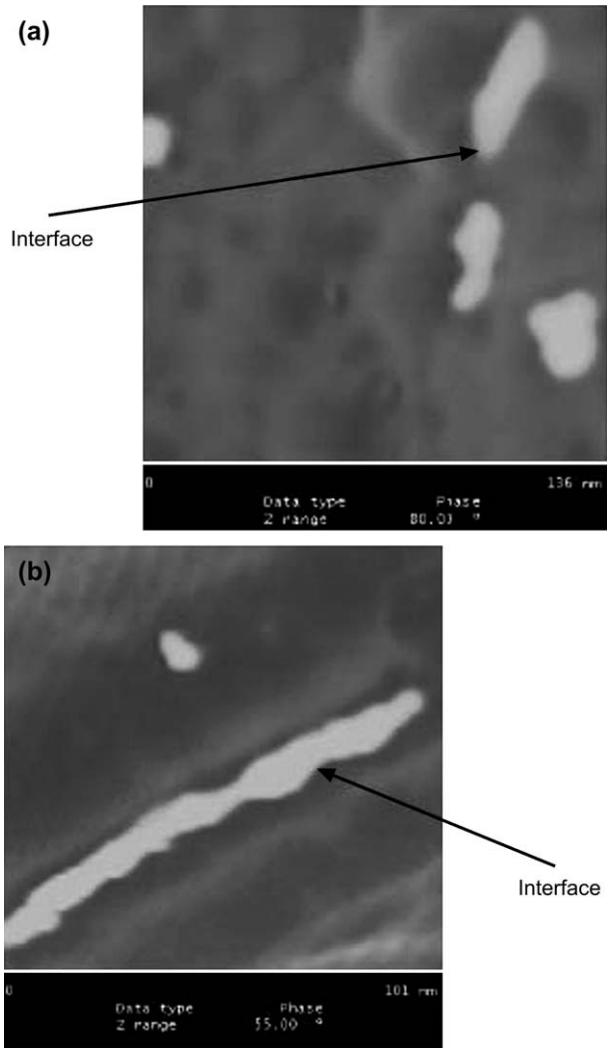

Fig. 8. Interface regions in (a) $F_{B5}C_{NA}4$ and (b) $F_{B5}C_{20A}4$.

filled sample, the interface region is more in the case of the unmodified clay filled sample. The thickness of the rubber shells was measured using the section analysis. The thickness of the rubber shell is 6 ± 2 nm and 2 ± 1 nm for $F_{B5}C_{NA}4$ and $F_{B5}C_{20A}4$, respectively. This may be due to the higher bound rubber in the case of $F_{B5}C_{NA}4$. This can be confirmed from the swelling study of the samples. The gel-fraction values (measured from the swelling studies reported in our earlier work) of $F_{B5}C_{NA}4$ (3.41) and $F_{B5}C_{20A}4$ (2.19) support the bound rubber concept [22].

The difference in particle size of the fillers and their distribution in the matrix can be attributed to the polymer–filler interaction. As the average particle size is smaller and the interface region is thicker in the case of the unmodified clay filled samples, the interaction of fluoroelastomer is more with NA. This may be due to the polar–polar interaction of the rubber with NA. Polar hydroxyl groups of the unmodified clay attract the chains of fluoroelastomer having $C^{\delta+}-F^{\delta-}$ bonds. In the modified clays, there are some long chain amines on the surface which induce some non-polarity to the clay. Thus, there is reduced interaction between the modified clays and the rubber. As, the unmodified clay is more compatible, the rubber shell surrounding the clay particles is also thicker and the interparticle distance is more in the case of $F_{B5}C_{NA}4$.

3.2. Roughness analysis

The RMS (R_q) and R_a values of the gum and the filled samples are included in Table 2. Before quantifying, the images were flattened using first-order flattening. Flattening removes image artifacts due to vertical (Z) scanner drift, image bow, skips, and anything else that may have resulted in a vertical offset between scan lines.

In the case of the neat rubber, RMS (R_q) value is found to be 1.53 nm and R_a is 1.18 nm. Generally, RMS (R_q) and R_a will be similar, if there is no large deviation from the mean surface level. The difference in the RMS (R_q) and R_a value of 0.35 nm suggests that there is not much undulation as expected for a neat rubber. In the case of $F_{B5}C_{NA}4$, RMS (R_q) is found to be 4.59 nm and R_a value is 3.65 nm. RMS (R_q) is found to be 5.18 nm and R_a value is 4.20 nm for $F_{B5}C_{20A}4$. The higher value of ($R_q - R_a$) (0.94 and 0.98 nm for the unmodified and the modified clay filled samples, respectively) with respect to the neat rubber confirms the presence of filler particles on the surface.

The main limitation of the roughness analysis is that it does not show the lateral spacings of the surface features. For detailed specific roughness properties, it is required to perform the spectral roughness analysis. The RMS roughness analysis gives only primary information about the fine-scale fluctuations in the effective surface height. Information about the intrinsic roughness distribution and the transverse properties at any frequency scale cannot be obtained from the above algorithm. The above limitation can be overcome by using power spectral density (PSD) analysis, which provides valuable information not only on the height deviation of the roughness profile but also on its lateral distribution.

The 2DPSD of the gum and filled samples are shown in Fig. 9a–c. With this technique it is possible to know how much is the contribution of a particular sized feature to an image. The total power is shown in Table 2. Compared to the neat rubber (F_{B5}), the intensity of spectral spikes is higher in the nanoclay loaded rubbers both in low and high frequency regions indicating a higher roughness in these systems. The total power as well as the equivalent RMS (square root of the total power) values support the above explanation. Since the fillers

Table 2
Quantitative parameters from nanocomposites and neat rubber

Parameters	F_{B5}	$F_{B5}C_{NA}4$	$F_{B5}C_{20A}4$
Average thickness of rubber shell (nm)	–	6 ± 2	2 ± 1
Average particle width (nm)	–	10 ± 3	15 ± 2
RMS (R_q) (nm)	1.53	4.59	5.18
R_a (nm)	1.18	3.65	4.20
Total power (nm^2)	1.10	18.90	27.10
Equivalent RMS (R_q) (nm)	1.05	4.35	5.27
Fractal dimension (D), (nm)	–	1.55	1.77

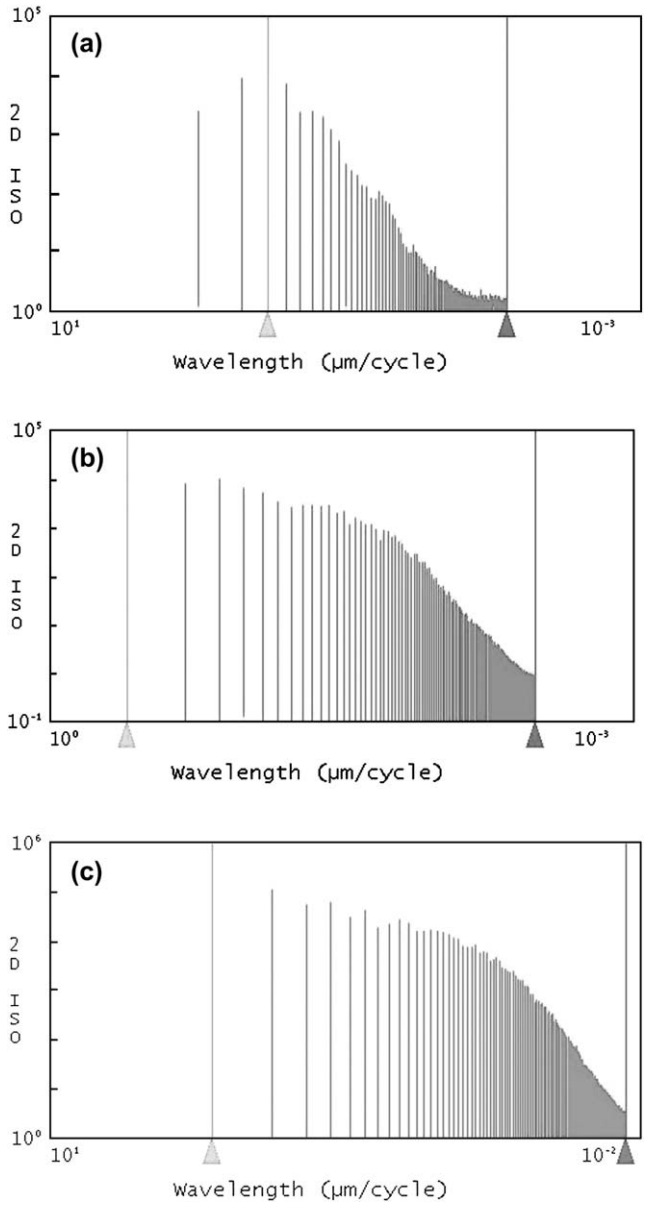

Fig. 9. Two-dimensional isotropic power spectral densities of (a) F_{B5}, (b) $F_{B5}C_{NA}4$, and (c) $F_{B5}C_{20A}4$.

are highly irregular in nature and have particles of various sizes, the surfaces of these samples are randomly rough.

3.3. Power spectral density

One-dimensional power spectral density (1DPSD) is calculated from 2DPSD expression by the Digital Instruments Nanoscope IIIa software. Surface parameter such as the fractal dimension is calculated from the 1DPSD, while qualitative analysis of two-dimensional periodicities is best achieved by 2DPSDs.

Plotting log (1DPSD) against log (frequency) reveals characteristic dimensions for the periodic surface in the form of peaks. The frequency value at the peak-center is related to the real space value of the wavelengths that define this periodic surface. A periodic surface indicates that there is no random roughness. The other case is of a self-affine surface. Each part of a self-affine object is an image of the whole object scaled differently in different directions [29]. This randomly rough surface has a transition point between frequency-independent nature and a self-similar behavior. Self-similarity is the most striking property of isotropic fractals, in which each piece of a shape is geometrically similar to the whole [30]. At low frequency the behavior is frequency-independent, whereas at high frequency the self-similar roughness is observed.

The constant slope-region of the PSD is described as self-similar and is a property of fractal objects [8,26]. A fractal object is a randomly rough surface, having irregularities of various sizes that bear a special ‘‘scaling’’ relationship to one another [31]. For a fractal object the power spectra is defined as [8]:

$$\mathrm{PSD}(f) = \frac{k_n}{f^l} \tag{7}$$

where, PSD is the one-dimensional power spectral density, f is the frequency, l is the slope and k_n is the intercept.

The fractal dimension is defined as

$$D = \frac{5 - l}{2} \tag{8}$$

Physically, fractal dimension, D describes how roughness fills the space.

Fig. 10 shows the plot of log (1DPSD) vs. log (spatial frequency). The figure reveals that the polymer–clay nanocomposites show a self-affine topography while the neat rubber film shows a peak indicating a periodic surface. Fractal dimension, D increases from 1.55 for $F_{B5}C_{NA}4$ to 1.77 for $F_{B5}C_{20A}4$ (Table 2). As the roughness variation can be correlated with the aggregated nature of filler, the higher value of D specifies the higher particle size of the modified clay, 20A.

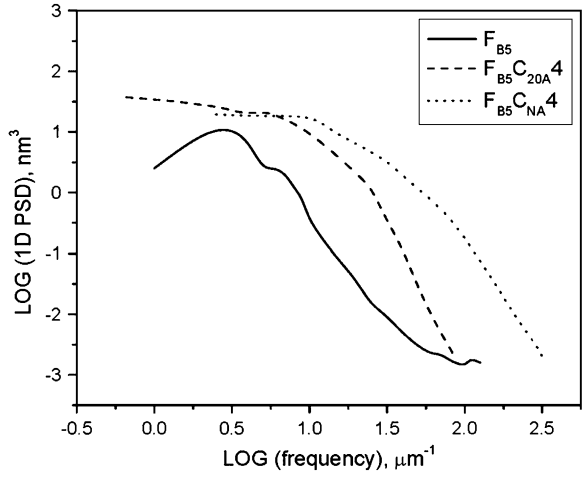

Fig. 10. Plot of one-dimensional power spectral density vs. spatial frequency.

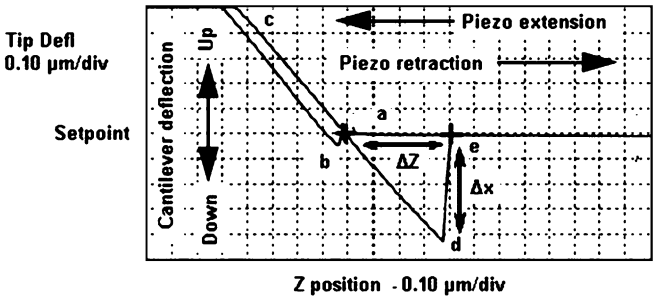

Fig. 11. A typical force-plot of the atomic force microscope.

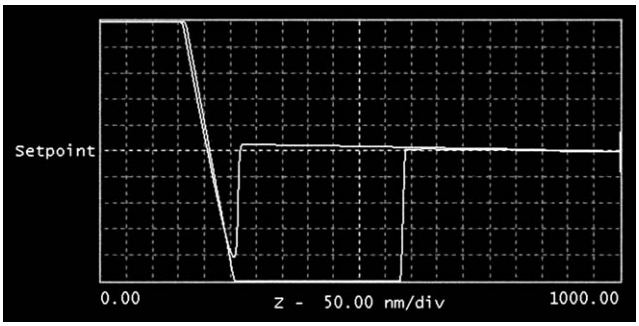

Fig. 12. Force-plot of F_{B5}.

3.4. Contact and adhesion force measurement

The contact and adhesion forces have been calculated from the force-plots obtained from contact mode AFM. A typical force-plot has been shown in Fig. 11: (a) Non-contact range, (b) jump-into-contact between probe and substrate, (c) maximum position of substrate, (d) maximum interaction force and (e) abrupt separation probe–substrate [32]. Adhesion force was calculated from the pull-off portion of the retracting curve (Δx) and the contact force calculated from horizontal distance traversed by piezo in Z-direction, ΔZ (shown in Fig. 11).

The contact force is defined by the equation:

$$F = k\,\Delta Z \tag{9}$$

where, k is the spring constant of the cantilever.

Adhesion and contact forces were calculated for the neat rubber and the unmodified clay filled rubber samples from the diagrams, shown in Figs. 12 and 13a–c. In the case of $F_{B5}C_{NA}4$, three different adhesion and contact forces are observed (Table 3). The highest value of adhesion and contact force observed here (11.1 ± 3.0 nN and 231.4 ± 3.0 nN), are similar to that of the neat rubber. Hence, this corresponds to the matrix. The least adhesion and contact force is observed on the filler particle as it is the hardest species on the sample. The intermediate values correspond to the interface region. These force calculations could not be done accurately in the case of $F_{B5}C_{20A}4$ as the interfacial width is very thin.

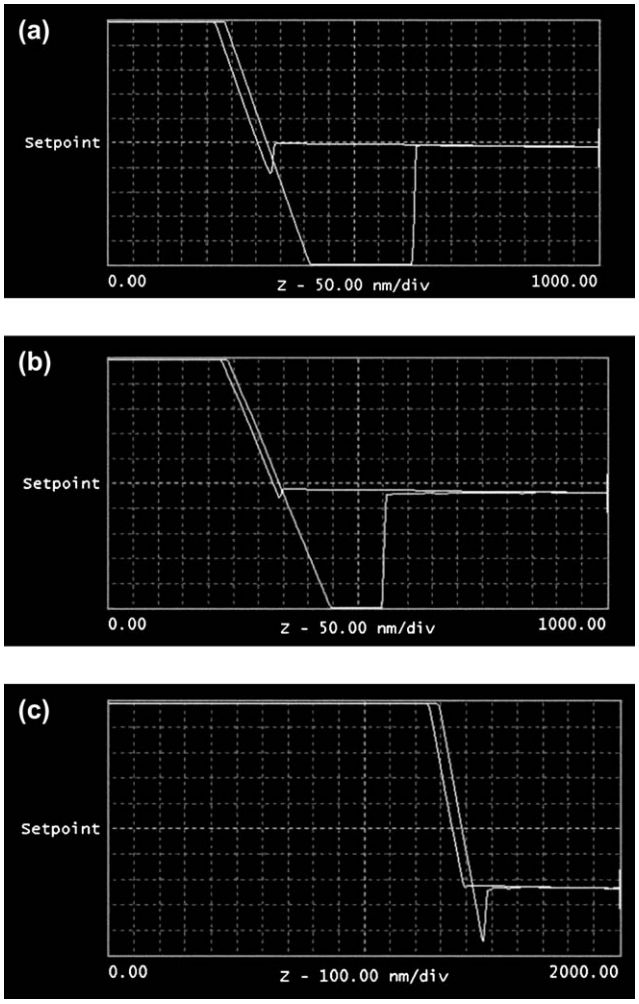

Fig. 13. Force-plots of $F_{B5}C_{NA}4$ (a) on the matrix, (b) on the interface, and (c) on the filler particle.

3.5. Explanations in terms of thermodynamics and SHAB theory

From the above quantitative discussion, it is clear that the filler particle size is higher in the case of the modified clay filled system. Hence, it is inferred that more particle breakdown was possible in the case of the unmodified clay filled system. The average particle size indicates exfoliation of the layered clay filler. All the above experimental results could be explained as given below. Enhanced interaction between NA and the rubber favors the nanocomposite formation which can be confirmed from the thermodynamics point of view. The free energy change of the system after mixing the clay in fluoroelastomers may be given as follows:

$$\Delta G_E = \Delta H_E - T\,\Delta S_E, \quad \text{for rubbers} \tag{10}$$

$$\Delta G_C = \Delta H_C - T\,\Delta S_C, \quad \text{for clays} \tag{11}$$

Therefore, total free energy change of the system is

$$\Delta G_S = \Delta H_S - T\,\Delta S_S = (\Delta H_E + \Delta H_C) - T(\Delta S_E + \Delta S_C) \tag{12}$$

Table 3
Adhesion and contact forces from force-plots

Sample	Region	Pull-off/adhesion force (nN)	Contact force (nN)
F_{B5}		11.0 ± 2.0	229.3 ± 2.0
$F_{B5}C_{NA}4$	Clay	4.6 ± 2.0	57.8 ± 4.0
	Interface	9.3 ± 5.0	159.7 ± 7.0
	Rubber	11.1 ± 3.0	231.4 ± 3.0

From the expression, ΔG_S value will be negative and hence the most favorable interaction between the clay and the rubber will take place when ΔH_S is negative and ΔS_S is positive.

ΔH_S has been calculated for different systems from the IR spectra using Fowkes's equation [22],

$$\Delta H = 0.236\,\Delta\nu \tag{13}$$

$\Delta\nu$ has been calculated from the peak shift in different clay filled systems, compared to the neat rubber. The change in the position of the peak at 1197 cm^{-1} has been considered as it is the characteristic peak of C–F bond, common in every sample. The values are reported in Table 4. ΔH_S is negative for $F_{B5}C_{NA}4$. But for the modified clay filled sample, it has small positive value. More negative ΔH_S value makes ΔG_S more negative. Hence, formation of $F_{B5}C_{NA}4$ is more favorable than the modified clay based nanocomposites.

When polymer chains enter into the gallery of the clay, they reside in a restrained form, i.e. ΔS_E is negative. In contrast, the expansion of the gallery by rubber chains causes the entropy change in the clay, ΔS_C to be positive. If the clays are exfoliated, this may probably compensate the entropy loss associated with the confinement of rubber chains.

When the fluoroelastomer is mixed with the unmodified clay, the polar clay attracts polar polymer molecules. The rubber chains enter into the smaller gallery-gap of this clay and its motion is restricted. So, ΔS_E is negative. But these chains break the layered structure of the clays (as we have observed from the morphology) making ΔS_C positive. This will compensate the entropy loss.

But the modified clays are having larger gallery-spacings (2.42 nm vs. 1.16 nm). So, more number of polymer chains can enter into the gallery-gap. Hence, more numbers of polymer molecules are restrained. So, ΔS_E will be more negative compared to that of unmodified clay. Moreover, it can be observed that the particle width is also higher in the case of 20A, indicating partial exfoliation (Fig. 2c). Therefore, $(\Delta S_E + \Delta S_C)$ value will be more positive in the case of the unmodified clay compared to modified clay filled systems.

As a result, the mixing of the unmodified clay with the fluoroelastomer will be more favorable than that of the modified one. Hence, we can observe smaller particles in the AFM micrograph of the unmodified clay based nanocomposites.

Table 4
Value of enthalpy change from IR spectra

Sample name	Peak position (cm^{-1})	ΔH (kcal/mol)
F_{B5}	1197	
$F_{B5}C_{NA}4$	1186	−2.60
$F_{B5}C_{20A}4$	1199	0.47

Moreover, in the unmodified clay, sodium ion is residing in the galleries of the clays, which is a hard acid. On the other hand, there are tertiary ammonium ions in Cloisite 20A, which are soft acid in nature. Fluoroelastomers contain $C^{\delta+}$–$F^{\delta-}$ bonds, where the $F^{\delta-}$ is a hard base in nature. So, it will be more attracted towards the hard acid [according to soft–hard acid base (SHAB) theory] [22]. So, polymer–filler interaction will be more in the case of the unmodified clays. Besides this, polar–polar interaction is also responsible for better polymer–filler interaction in the case of unmodified clays as discussed earlier and evident from peak shift in the IR spectra.

4. Conclusions

The present study utilized AFM as an investigating tool to observe the morphology of the fluoroelastomer-clay nanocomposites, the dispersion of the nanoclays in the rubber matrix, interface thickness, and interaction forces. The phase images of the filled nanocomposites revealed the presence of clay fillers as the bright features in the dark rubber matrix. Smaller particle size of the unmodified clay than that of the modified clay was apparent. The results obtained from section analysis and filler distribution histogram confirmed the above findings. The polymer–filler interaction was stronger in the case of unmodified clay filled sample. The PSDs presented in this study revealed the self-affine nature of surfaces created by addition of nanoclays. Using 1DPSDs and 2DPSDs, SPM data of different nanocomposites were evaluated qualitatively and quantitatively to develop an understanding of the influence of different nanoclays on the morphology. In addition, fractal analysis calculated from 1DPSD, showed lower fractal dimension in the case of $F_{B5}C_{NA}4$ than that of $F_{B5}C_{20A}4$. All types of analysis reflected the fact that the unmodified clay filler had better interaction with the fluoroelastomers than the modified organo-clays. The morphological features were also explained from thermodynamic point of view and SHAB theory.

References

[1] Sinha Ray S, Okamoto M. Prog Polym Sci 2003;28:1539.
[2] Sadhu S, Bhowmick AK. J Polym Sci Part B Polym Phys 2004;42:1573.
[3] LeBaron PC, Wang Z, Pinnavaia TJ. Appl Clay Sci 1999;15:11.
[4] Vaia RA, Ishii H, Giannelis EP. Chem Mater 1993;5:1694.
[5] Lan T, Pinnavaia T. J Chem Mater 1999;6:2216.
[6] Cho JW, Paul DR. Polymer 2001;42:1083.
[7] Binnig G, Quate CF, Gerber CH. Phys Rev Lett 1986;56:930.
[8] Sanmugharaj AM, Bandyopadhyay S, Roy S, Bhowmick AK. J Adhes Sci Technol 2003;17:1167.
[9] Roy S, Bhowmick AK, Bandyopadhyay S. Rubber Chem Technol 2003;76:1091.
[10] Reichert P, Nitz H, Klinke S, Brandsch R, Thomann R, Muelhaupt R. Macromol Mater Eng 2000;275:8.
[11] Dietsche F, Thomann Y, Thomann R, Muelhaupt R. J Appl Polym Sci 2000;75:396.
[12] Sadhu S, Bhowmick AK. J Mater Sci 2005;40:1633.
[13] Mirabella Jr FM. Abstracts of papers, 224th ACS National Meeting, Boston, MA, United States, August 18–22; 2002.
[14] Kuan H, Ma CM, Chuang W, Su H. J Polym Sci Part B Polym Phys 2005;43:1.

[15] Li Xiaodong, Gao Hongsheng, Scrivens Wally A, Fei Dongling, Thakur Vivek, Sutton Michael A, et al. Nanotechnology 2005;16:2020.
[16] Jiang Tao, Wang Yu-Hua, Yeh Jen-Taot, Fan Zhi-Qiang. Eur Polym J 2005;41:459.
[17] Park H, Liang X, Mohanty AK, Misra M, Drzal LT. Macromolecules 2004;37:9076.
[18] Malwitz MM, Dundigalla A, Ferreiro V, Butler Paul D, Henk MC, Schmidt G. Phys Chem Chem Phys 2004;6:2977.
[19] Hu X, Lesser AJ. Polymer 2004;45:2333.
[20] McNally T, Raymond MW, Lew CY, Turner RJ, Brennan GP. Polymer 2003;44:2761.
[21] Clement F, Lapra A, Bokobza L, Monnerie L, Menez P. Polymer 2001;42:6259.
[22] Maiti M, Bhowmick AK. J Polym Sci Part B Polym Phys 2006;44:162.
[23] Maiti M, Bhowmick AK. J Appl Polym Sci 2006;101:2407.
[24] Command Reference Manual. Digital Instruments Veeco Metrology Group; 2001 [chapter 14].
[25] Skolnik AM, Hughes WC, Augustine BH. Chem Educator 2000;5:8.
[26] Buchko CJ, Kozlo KM, Martin DC. Biomaterials 2001;22:1289.
[27] Magonov SN, Ellings V, Whangbo MH. Surf Sci 1997;375:L385.
[28] Markiewiez P, Goh MC. J Vac Sci Technol B 1995;13:1115.
[29] Sapozhnikov V, Foufoula-Georgiou E. J Phys A Math Gen 1995;28:559.
[30] Mandelbrot B. The fractal geometry of nature. New York: Freeman and Company; 1983.
[31] Mandelbrot B, Oassoja DE, Paullay AJ. Nature 1984;308:721.
[32] Sindel U, Zimmermann I. Powder Technol 2001;117:247.